Propagating Polaritons in III-Nitride Slab Waveguides

J. Ciers,* J. G. Roch,† J.-F. Carlin, G. Jacopin, R. Butté, and N. Grandjean

Institute of Physics, École Polytechnique Fédérale de Lausanne (EPFL), CH-1015 Lausanne, Switzerland

(Received 7 November 2016; revised manuscript received 9 February 2017; published 24 March 2017)

We report on III-nitride waveguides with *c*-plane GaN/(Al, Ga)N quantum wells in the strong light-matter coupling regime supporting propagating polaritons. They feature a normal-mode splitting as large as 60 meV at low temperatures thanks to the large overlap between the optical mode and the active region, a polariton decay length up to 100 μm for photonlike polaritons and a lifetime of 1 to 2 ps, with the latter values being essentially limited by residual absorption occurring in the waveguide. The fully lattice-matched nature of the structure allows for very low disorder and high in-plane homogeneity, which is an important asset for the realization of polaritonic integrated circuits that could support nonlinear polariton wave packets up to room temperature thanks to the large exciton binding energy of 40 meV.

DOI: 10.1103/PhysRevApplied.7.034019

I. INTRODUCTION

Over the past 15 years, optical interconnects, which are essential building blocks for the realization of photonic platforms fully integrated on a chip—so-called photonic integrated circuits (PICs)—have triggered huge interest due to their promising potential in the field of information technology for the realization of small-footprint low-energy devices that may also offer a high clock rate and may eventually support strong nonlinearity [1].

Among the various systems at play, one such interesting platform deals with exciton polaritons, hereafter called polaritons, in the waveguide geometry. Polaritons are quasiparticles that arise from the hybridization between a (confined) photon mode and a semiconductor exciton in the so-called strong-coupling regime (SCR) [2]. Their properties are therefore intermediate between those of photons and excitons, and as such they benefit from the best of both worlds. Polaritons can propagate at near light speed and interact through their exciton fraction. This feature makes them ideal candidates for low-power active all-optical devices such as switches, optical transistors, and logic gates [3,4]. One of the inherent difficulties with all-optical devices is the lack of interaction between photons, which makes it nearly impossible to directly modify a light beam with a second one. To operate a nonlinear all-optical device made from traditional dielectric materials, very high intensities are required, with typical values for the nonlinear refractive index on the order of 10^{-16} cm^2/W [5], and present plasmonic alternatives are inherently lossy [6]. A polariton-based device, however, combines a strong nonlinearity—on the order of 10^{-10} cm^2/W—with a very fast response time on the order of a few picoseconds [4,7].

In order to reach the SCR between excitons and photons and maximize the normal-mode splitting Ω_{Rabi} between polariton eigenmodes, it is paramount to reduce any source of decoherence and maximize the exciton-photon coupling strength g_0. For a confined optical mode coupled to quantum-well (QW) excitons [8], it can be expressed as [9,10]

$$g_0 = \hbar\sqrt{\frac{e^2 N_{\mathrm{QW}}^{\mathrm{eff}} f_X}{2m_0\varepsilon_0 n_{\mathrm{eff}}^2 L_{\mathrm{eff}}}}, \tag{1}$$

where $\hbar$ is the reduced Planck constant, e is the elementary charge, $N_{\mathrm{QW}}^{\mathrm{eff}}$ is the effective number of QWs (i.e., the nominal number of QWs weighted by the intensity of the optical mode profile) that are coupled to the optical mode, f_X is the oscillator strength per unit area of the QW exciton, m_0 is the free-electron mass, ε_0 is the permittivity of vacuum, n_{eff} is the effective refractive index of the optical mode and L_{eff} is the corresponding modal effective length [11]. From this equation, we can see the interest in using QWs supporting large-oscillator-strength excitons and promoting structures with a large $[(N_{\mathrm{QW}}^{\mathrm{eff}})/L_{\mathrm{eff}}]$. In addition, in order to maintain the SCR up to room temperature or above, the QW excitons should be stable at these elevated temperatures. This requirement favors direct wide-band-gap semiconductors, which naturally have large exciton binding energies.

As previously mentioned, the waveguide geometry is a promising platform for strong-coupling applications [12–17]. Indeed, the high in-plane group velocity on the order of 10^7 m/s in waveguides makes them attractive for the achievement of fast PICs. Optical confinement provided by total internal reflection (TIR) results in smaller optical leakage and a small L_{eff} value compared to distributed-Bragg-reflector (DBR) confinement traditionally used in planar microcavities (MCs) or quasi-one-dimensional

*joachim.ciers@epfl.ch

†Present address: Nano-Photonics Group, University of Basel, CH-4056 Basel, Switzerland.

MCs [18,19]. This is particularly the case for III-nitrides, as the refractive-index contrast between materials is low. The present III-nitride waveguide—as detailed below—supports a mode with an effective length of 175 nm, whereas a comparable III-nitride MC has an effective length of 590 nm [20]. A waveguide is also more robust against any deviations in layer thickness compared to MCs since a guided mode does not depend on the cladding thickness and depends only slightly on the core dimensions, hence leading to higher fabrication yields. Additionally, the waveguide geometry can allow for easy potential landscaping by electrical gating [17] and the electrical injection of carriers—as is commonly done in edge-emitting laser diodes (LDs)—as opposed to electrical injection through DBRs, which is a much more challenging task. As an illustration of the potential of strongly coupled waveguides, let us note that nonlinear effects relying on the formation of dark-bright spatiotemporal polariton-soliton wave packets with energies as low as 0.5 pJ has recently been reported in GaAs-based structures operating at 10 K [7].

In this work, we report on a III-nitride slab supporting waveguided polaritons originating from the hybridization of GaN/(Al, Ga)N multiple-QW (MQW) excitons with the propagating TE_0 optical mode. Waveguided polaritons are monitored up to 100 K with a normal-mode splitting of approximately 60 meV. The guided polaritons propagate with a decay length of about 100 μm and have a lifetime of 1 to 2 ps. The sample structure is first discussed in Sec. II. The properties of the bare QW excitons and the guided polaritons are then analyzed in Secs. III and IV, respectively. The main conclusions and an outlook toward future work are given in Sec. V.

II. SAMPLE STRUCTURE

The structure under investigation is sketched in Fig. 1(a) and consists of a 130-nm-thick active region with 22 $GaN/Al_{0.1}Ga_{0.9}N$ (1.5 nm/3.5 nm) QWs sandwiched between a 400-nm-thick $Al_{0.83}In_{0.17}N$ bottom cladding that is lattice matched to GaN and a 100-nm-thick SiO_2 top cladding. The bottom cladding and the active region are grown by metal-organic vapor-phase epitaxy in an AIXTRON 200/4 RF-S reactor on a low-dislocation-density (10^6 cm^{-2}) freestanding (FS) c-plane GaN substrate. High-quality (Al,In)N layers have been demonstrated on these substrates [24,25] and have been successfully used for optical mode confinement in the waveguide region of visible III-nitride edge-emitting LDs [26]. The (Al,In)N bottom cladding layer contains seven 5-nm-thick GaN interlayers positioned 50 nm apart in order to avoid kinetic roughening of the (Al,In)N alloy [25]. Note that the effect of the quantum-confined Stark effect on the exciton oscillator strength is negligible due to the reduced thickness (1.5 nm) of the present GaN/(Al, Ga)N QWs and the low Al content in the barriers [27]. This result is confirmed by the elevated value of 0.8 for the electron-hole overlap integral for these QWs, as calculated with the $k \cdot p$ formalism (see Sec. III for further details). In addition, the use of an (Al,Ga)N barrier width of 3.5 nm avoids any coupling between adjacent wells. All aforementioned layer thicknesses are measured by high-resolution x-ray diffraction (HR-XRD) [11].

A significant advantage of the polariton waveguide geometry over the more conventional planar MC design employing similar GaN/(Al, Ga)N QWs is that the bottom cladding can be grown lattice matched to the FS GaN substrate. Indeed, in the MC case, a substantial Al concentration is required in the two quarter-wave layers of the bottom UV DBR to avoid unwanted absorption at the GaN QW energy [20]. The resulting lattice mismatch between the GaN template and the UV (Al, In)N/(Al, Ga)N DBR requires the implementation of specific strain-engineering solutions to avoid the formation of cracks [28] and leads to a higher density of defects, mainly threading dislocations,

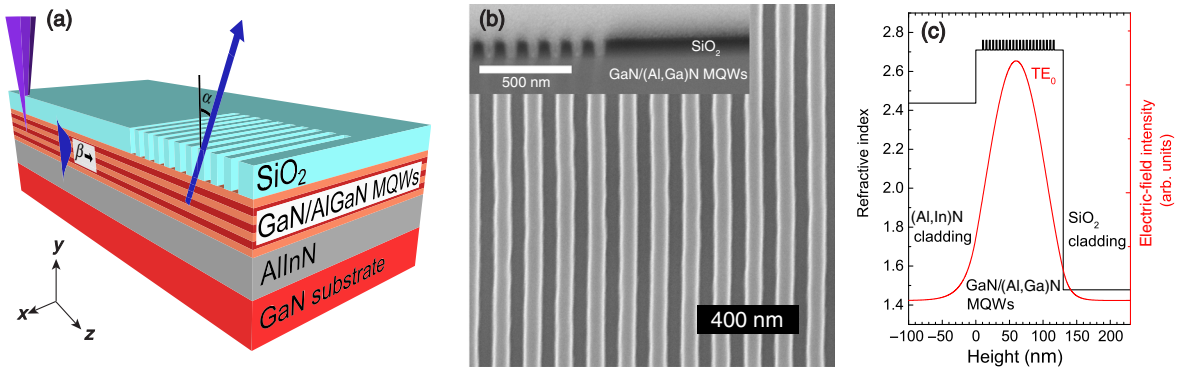

FIG. 1. (a) Sketch of the sample structure. (b) SEM of the fabricated gratings. Top view and (inset) cross-section view. The cross section is prepared by focused-ion-beam milling and the image is corrected for sample tilt. (c) Optical mode profile of the TE_0 mode supported by the present waveguide. This mode profile is calculated with a finite-difference time-domain mode solver [21]. The refractive index for GaN and (Al,Ga)N are taken from the work of Brunner *et al.* [22], the refractive index of (Al,In)N is taken from Butté *et al.* [23], and the refractive index of SiO_2 is taken from experimental data.

as there would be no additional benefit in using FS GaN substrates in the latter case. The entire present structure is pseudomorphic to the FS GaN substrate, as confirmed by HR-XRD reciprocal-space mapping [11].

The SiO_2 top cladding is deposited by plasma-enhanced chemical vapor deposition on top of the active region. In order to outcouple the guided modes from the waveguide for subsequent analysis, a grating coupler is defined in the top cladding [29] by electron-beam lithography using a 100-keV Vistec EBPG5000 *e*-beam lithography system and a ZEP520A positive resist, and inductively coupled plasma etching with CHF_3/SF_6 chemistry. A scanning electron micrograph (SEM) of the fabricated structure in top and cross-section views is shown in Fig. 1(b). The etched sidewalls form an angle of 3° with the vertical. The aspect ratio of the etched slits is 5:3. The gratings have a period Λ of 125 nm, with 50% fill factor, and span over a $100 \times 100\ \mu m^2$ area.

We can relate the propagation constant β of the guided mode to the emission angle α [shown in Fig. 1(a)] from the grating output coupler by the relation

$$k_{z,\mathrm{air}} = \frac{\omega}{c}\sin\alpha = \beta - \frac{2\pi q}{\Lambda}, \tag{2}$$

where $q \in \mathbb{Z}$ is the diffraction order. We use a first-order grating to maximize the outcoupled light intensity. The grating period is chosen such that the central in-plane wave vector of interest ($50\ \mu m^{-1}$) is emitted perpendicular to the sample.

A slab waveguide can support both transverse-electric [(TE), with the electric field along x] and transverse-magnetic [(TM), with the magnetic field along x and the electric field in the y-z plane] guided modes. We define z as the propagation direction of the guided modes, y as the growth direction of the sample, and x as the direction perpendicular to both [as shown in Fig. 1(a)]. The thickness of the waveguide core is chosen such that only the TE_0 and TM_0 modes are supported and all higher-order modes are cut off. This cutoff prevents the excitons from coupling to multiple modes, which would act as a lossy channel for the photogenerated carriers. The X_A exciton couples exclusively, as X_B mostly does, to the in-plane electric field as deduced from $k \cdot p$ calculations, which favors the TE mode over the TM one. The overlap integral of the E_z field of the TM_0 mode with the active region is almost 2 orders of magnitude smaller than the overlap integral of the TE_0 E_x field with the active region. Therefore, we consider only the TE_0 mode in the remaining part of this work.

The present structure is optimized to maximize the light-matter coupling strength g_0 between the guided photons and the MQW excitons. The high number of QWs (22) combined with the large overlap between the optical mode and the QWs—the TE_0 mode has no nodes and the mode intensity quickly decreases outside the active region, as can be seen in Fig. 1(c)—and the large oscillator strength of the QWs result in a high g_0 value of 30 meV.

III. BARE QUANTUM-WELL PROPERTIES

In the present structure, three different light-matter coupling regimes can potentially coexist in distinct zones of the energy vs β diagram, as shown in Fig. 2. Photons with an in-plane wave vector outside the active region light cone do not exist; hence, explaining the terminology dark excitons as the radiative recombination of excitons in this region is forbidden. In the k-space region between the bottom-cladding and the active-region light cone, photons are tightly confined in the waveguide by TIR and, as is shown in Sec. IV, they hybridize with the X_A excitons. Inside the bottom-cladding light cone, TIR is lost at the bottom interface and the active region becomes a lossy resonator with broad optical modes. Therefore, excitons and photons are weakly coupled in this region. Inside the top-cladding light cone, TIR is also suppressed at the top interface and the structure forms a low-quality-factor (Q) Fabry-Perot resonator. As a result, we simultaneously have three populations of excitations in the sample under cw nonresonant excitation: dark excitons, waveguided polaritons, and weakly coupled excitons. The latter population allows us to probe the bare excitonic properties inside the

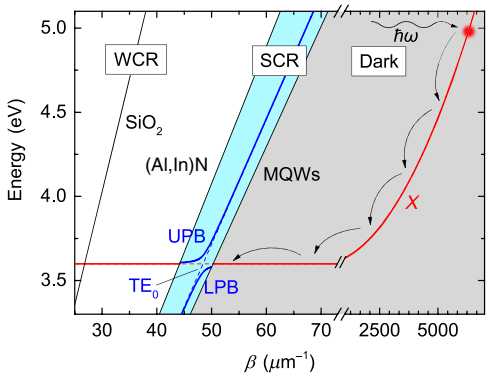

FIG. 2. Eigenmode dispersion of the present structure for polarization along x. The light cones of the multiple quantum wells (MQWs), bottom cladding [(Al,In)N] and top cladding (SiO_2) are represented in black. They mark the transitions between the different light-matter coupling regimes. The dark regime occurs outside the active-region light cone (marked in gray), where photons do not exist. Between the active-region and the bottom-cladding light cone, the exciton (X, red) and TE_0 guided mode are in the strong-coupling regime (SCR, blue) and form an upper (UPB) and a lower polariton branch (LPB). Within the bottom-cladding light cone, photons are poorly confined and couple weakly with the excitons (WCR, white). For simplicity, refractive-index dispersion is neglected in this plot. The considered optical refractive-index values are those expected at 3.6 eV (2.756 for the active region [22], 2.42 for the bottom cladding [23], and 1.47 for the top cladding). The exciton dispersion is calculated within the effective-mass approximation.

air light cone using conventional optical spectroscopy techniques.

We calculate the confined MQW electron and hole energy levels at 0 K using the $k \cdot p$ formalism [11,30] adapted for the analysis of strained MQW structures. Because of the geometrical effect in the MQW, the value of the electric field found by setting the potential difference between the extremities of the active region to zero amounts to 220 kV/cm in the (Al,Ga)N barriers and −625 kV/cm in the GaN wells, respectively [31]. An excitonic energy $E_{X_A} = 3.566$ eV and $E_{X_B} = 3.576$ eV is obtained for X_A for X_B, respectively, assuming an exciton binding energy of 40 meV in both cases. The latter is deduced from the variational approach developed by Leavitt and Little [32]. The relative oscillator strength of the X_A (0.5 for light polarized along both x and z, 0 along y) and X_B excitons (0.495 for light polarized along both x and z, 0.01 along y) shows an exclusive coupling for X_A and a heavily preferential coupling for X_B to the in-plane electric field components. Hence, it explains the poor excitonic coupling to the TM modes supported by the waveguide.

The bare exciton properties are experimentally investigated by photoreflectance (PR) and microphotoluminescence (μ-PL) spectroscopy [11]. Clear signatures can be observed in the low-temperature PR spectrum [shown in Fig. 3(a)] for the X_A and X_B QW excitons as well as the X_A barrier exciton. No signature of the underlying FS GaN substrate is observed in PR as, with this technique, the modulation induced by photogenerated carriers essentially occurs in the topmost layers. The critical points are fitted using the approach introduced by Aspnes [33,34]. The comparison between low-temperature PL and PR spectra [Fig. 3(a)] reveals a Stokes shift of 13 meV, which is similar to that previously reported for equivalent GaN/(Al, Ga)N MQW samples [34]. Note that since the PL and PR measurements are conducted with the sample in different cryostats, there is an uncertainty of approximately 500 μm—comparable to the PR spot size—on the relative sample location probed in both experiments. On the low-temperature PL spectra, we can clearly identify the X_A MQW exciton together with its first and second longitudinal-optical (LO)-phonon replicas, each separated by approximately 92 meV, the accepted LO-phonon energy for GaN. An inhomogeneous broadening of 8 meV is measured at 4 K for the X_A peak. This very low value for a sample that consists of 22 QWs indicates the high quality of the latter, which compares favorably with state-of-the-art GaN/(Al, Ga)N QW samples [34–36]. On the low-energy side of the X_A exciton, we observe a shoulder which is likely due to a bound excitonic state, X_{bound}. It could originate from the incorporation of acceptorlike impurities such as carbon during the low-temperature growth of the MQWs [37,38]. At low temperatures, a third peak is present at approximately 3.55 eV. This energy corresponds to the maximum of the polariton emission—see below—and, as such, this peak could be the signature of scattered lower polaritons.

The temperature dependence of the X_A transition can be well described by the expression [39]

$$E_{X_A}(T) = E_{X_A}(0) - \frac{2\alpha_B}{\exp(\Theta_B/T) - 1}, \tag{3}$$

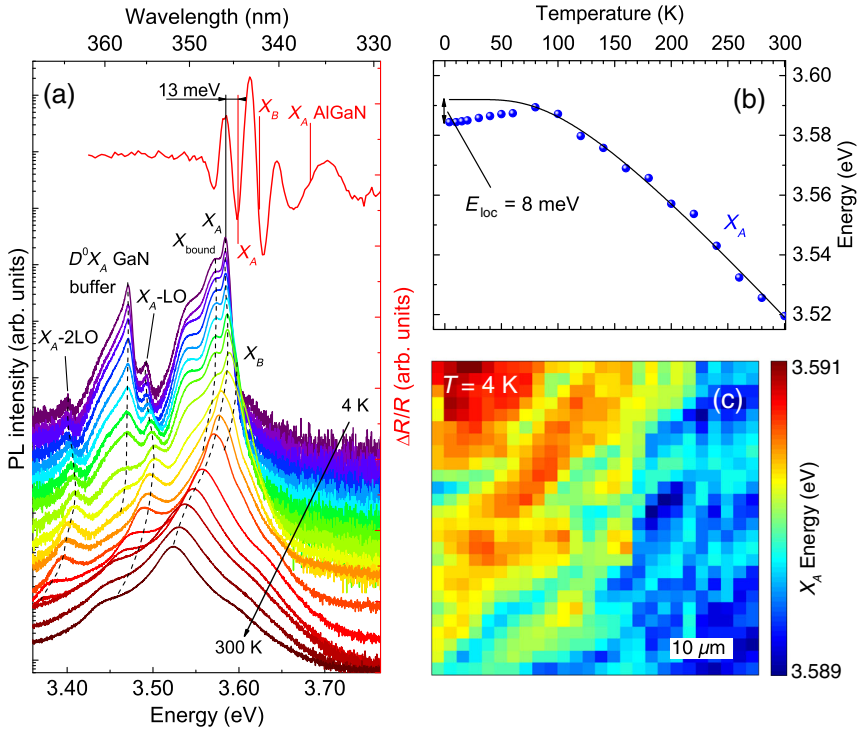

FIG. 3. (a) Low-temperature ($T = 10$ K) PR spectrum (red curve) and temperature series between 4 and 300 K of μ-PL spectra taken at approximately the same location showing a Stokes shift of 13 meV. The spectra are vertically shifted for clarity. (b) Temperature dependence of the X_A energy for the PL measurements shown in (a), together with a fit according to Eq. (3) (black curve). (c) μ-PL mapping of the X_A emission energy measured at 4 K. The observed standard deviation is as low as 0.42 meV over a 50×50 μm^2 area.

where $E_{X_A}(0)$ is the expected energy of the free-X_A-exciton transition at 0 K and the second term is the Bose-Einstein occupation factor for phonons where α_B is the electron-phonon coupling constant and Θ_B is the average phonon temperature. This model is notably more accurate than Varshni's empirical law at low temperature [22]. Upon fitting the measured PL emission energies to Eq. (3) [Fig. 3(b)], we find a localization energy of 8 meV, together with values of 70 meV and 322 K for α_B and Θ_B, respectively. The values for the latter two parameters are in good agreement with those reported by Brunner *et al.* for bulk (Al,Ga)N layers [22].

The energy of the X_A free exciton deduced from PR measurements (3.599 eV at 10 K) and Eq. (3) (3.592 eV at 4 K) is slightly higher than that originally expected from $k \cdot p$ calculations (3.566 eV). This result could be accounted for by assuming a smaller value of the built-in electric field in the MQWs and slightly different in-plane carrier masses.

The in-plane homogeneity of the sample is checked through μ-PL mapping performed at 4 K [Fig. 3(c)], which leads to a standard deviation σ as low as 0.42 meV for the X_A energy over a 50×50 μm^2 area. This finding shows the high degree of homogeneity of the sample, which is an important asset for the control of waveguided polaritons and the potential realization of PICs relying on such an approach. The uniformity of those waveguide samples can likely be ascribed to the growth performed on a low-defect-density FS GaN substrate, as the latter samples are expected to be much less affected by in-plane disorder than their strongly coupled counterparts grown on *c*-plane sapphire substrate [35,40].

To summarize this section, the low values of the inhomogeneous PL broadening (8 meV), the localization energy (8 meV), the Stokes shift (13 meV), and the in-plane inhomogeneity ($\sigma = 0.42$ meV) highlight the high quality and the homogeneity of the present sample, especially when taking into account the large number of QWs.

IV. GUIDED POLARITONS

The waveguide-dispersion curve is measured for various propagation distances by moving the excitation spot away from the grating outcoupler between 4 and 100 K. The measured signal intensity is relatively weak, for two reasons. First, only excitons lying outside the cladding light cone are expected to form polaritons, as shown in Fig. 2; hence, the fraction of excitons which relaxes into this light cone does not contribute to the signal. Second, as the slab waveguide is radially symmetric, waveguided polaritons, if present, will propagate isotropically from the excitation spot. Therefore, only polaritons within the angle covered by the collection zone can contribute to the signal and its intensity will approximately decrease as the reciprocal of the propagation distance r. This approximation holds well if the size of the collection region is substantially smaller than the propagation distance. Here, the collection region is 19 μm and the propagation distances used in the experiments range between 30 and 200 μm. A sketch to illustrate this outspread can be found in Fig. S4 of the Supplemental Material [11]. Additionally, the internal quantum efficiency of the active medium decreases with increasing temperature, which further reduces the signal intensity at higher temperatures. Above 100 K, the signal intensity becomes too weak to perform any reliable measurements. Note, however, that this weak intensity does not imply that the SCR could not be maintained above 100 K. The detected signal intensity could be significantly increased by using resonant excitation, which would couple most of the pump power into the waveguide polariton states, and by implementing ridge structures for lateral confinement. This approach would circumvent the current limitations of our measurements and likely allow for polariton propagation studies up to 300 K or above. One should also point out that the absorption losses occurring in the waveguide could be reduced by increasing the Al content in the QW barriers while preserving the QW optical quality, i.e., by controlling the amount of extra inhomogeneous broadening [35].

An example of a dispersion curve measured at $T = 4$ K is shown in Fig. 4, where the background signal coming from bare excitons is removed for clarity. The raw-measurement data as well as measurements taken at 100 K can be found in the Supplemental Material [11]. We clearly see a pronounced curvature in the measured signal, which is ascribed to the avoided crossing of lower polaritons with the uncoupled free X_A transition [41]. We compare the measured signal at 4 K to both a simple coupled-oscillator model (COM) and full two-dimensional finite-difference-time-domain (2D FDTD) calculations [11]. The COM uses a constant value of n_{eff} and, therefore, a linear dispersion for the uncoupled TE_0 waveguide mode. By fitting this model [the results are shown in Fig. 4(a)], we find a normal-mode splitting of 100 meV for this measurement. Application of Eq. (1) results in an oscillator strength of 3.0×10^{13} cm^{-2} for the QW excitons. The 2D FDTD calculations, on the other hand, take the material refractive-index dispersion into account. The resulting uncoupled TE_0 mode is curved due to the increase in refractive index of the QWs and the barriers near the band edge, located at 3.64 and 3.71 eV, respectively, as shown in Fig. 4(b). The 2D FDTD calculations are performed for various values of f_X, and a good fit to the data is found for $f_X = 1.1 \times 10^{13}$ cm^{-2}. The corresponding normal-mode splitting is 63 meV. The discrepancy in the values of f_X and Ω_{Rabi} between the COM and the 2D FDTD calculations is mainly due to the neglected refractive-index dispersion in the former case. Since the uncoupled mode is bent in the same direction as the anticrossing by the increasing refractive index toward the band edge, a smaller oscillator strength is required to reproduce the measured dispersion.

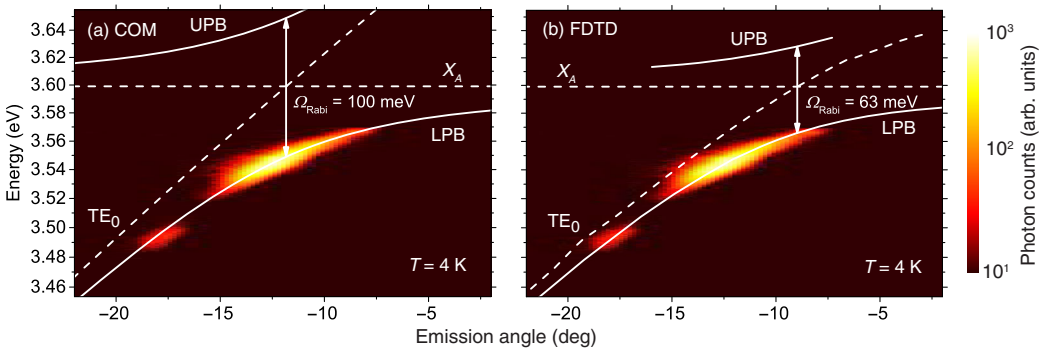

FIG. 4. Measured polariton dispersion for a propagation distance of 55 μm measured at $T = 4$ K, with an excitation power density of 640 W/cm^2. The background signal from the bare excitons is subtracted for clarity [11]. (a) A conventional COM is fitted to the data and the resulting UPB and LPB are shown in white, together with the uncoupled exciton (X_A) and the TE_0 mode. This model leads to a normal-mode splitting of 100 meV. (b) Full 2D FDTD mode calculations are performed for various values of the exciton oscillator strength. A good correspondence with the measurement is found for $f_X = 1.1 \times 10^{13}$ cm^{-2} (shown in white). We find a normal-mode splitting of 63 meV using this method. The same experimental data are shown in both (a) and (b).

A COM featuring a constant effective refractive index, therefore, systematically overestimates the exciton oscillator strength and the normal-mode splitting. This comparison shows the importance of the effect of the refractive-index dispersion in the analysis of photonic structures operating near the band edge. Note that a value of $f_X = 2.1 \times 10^{13}$ cm^{-2} was previously reported for similar QWs embedded in a strongly coupled MC using transfer-matrix simulations accounting for dispersion [34]. Let us point out that the observed curvature in the dispersion cannot be explained by the increase in the refractive index of the active region near the band gap, as can be seen in Fig. 4(b), which confirms that the present structure is operating in the SCR.

The signal intensity from the highly excitonic tail of the LPB is negligible in all measurements, most likely because the polaritons relax to lower energy states and because the outcoupling rate is proportional to their photon fraction. The photonic tail of the LPB is hardly visible in the measured polariton dispersions, likely due to the relaxation bottleneck of highly photonic polaritons [42]. Note that there is a second maximum in the polariton emission intensity at approximately 92 meV below the localized X_A emission energy. This finding could be explained by the LO-phonon-assisted relaxation of excitons to the LPB, as was already reported in the planar MC case [43].

By comparison with the 2D FDTD calculations, we find a normal-mode splitting of 63 meV for the curve measured at 4 K [Fig. 4(b)], and an average splitting of 60 meV between 4 and 100 K. Such a value has to be compared to the 56–60 meV reported by Christmann *et al.* for a III-nitride planar MC containing 67 GaN/(Al, Ga)N QWs [44]. The similar value of Ω_{Rabi} recorded for the two geometries is the direct manifestation of the increased $[(N_{\mathrm{QW}}^{\mathrm{eff}})/L_{\mathrm{eff}}]$ value in waveguide structures. We can compare the present values of the normal-mode splitting to the reported values of 5 to 6 meV in the case of a single QW GaAs-based polariton waveguide [14], and 290 meV in the case of excitons in organic semiconductors coupled to Bloch surface waves [15]. The difference between these values is essentially coming from the difference in f_X.

The absence of the UPB in the PL spectra is a well-known feature of wide-band-gap systems [20,45], which is mainly due to absorption occurring above the MQW band gap and the large Ω_{Rabi} value, which hinders the thermal promotion of polaritons to the UPB [42]. However, let us note that even in GaAs-based polariton waveguides, the UPB luminescence is usually rather weak—or even absent [14,17,46].

We did not observe any renormalization effects, i.e., any decrease in the normal-mode splitting, with increasing pumping power up to 6 kW/cm^2. This is the case because we cannot measure any dispersion relation for propagation distances shorter than 20 μm. For these short distances, the outcoupled guided light is not distinguishable from the very intense direct PL signal originating from the MQWs inside the air light cone. Therefore, we essentially probe regions where the reduction in the polariton density coming from their radial outspread is significant and where renormalization should not be expected [40,47].

In addition to the above-mentioned temperature dependence, the observed decrease in the signal intensity with increasing propagation distance is not only due to the radial spread out of waveguided polaritons from the excitation spot—which leads to a decrease in the polariton density overlapping with the collection area as r^{-1}—but also to polaritonic decay. Indeed, as waveguided polaritons propagate, they experience an intrinsic decay following an exponential Beer-Lambert law, mainly due to photonic losses for the present exciton-photon detunings (δ). In order to determine their intrinsic decay length—defined as the distance over which the integrated polariton PL intensity at

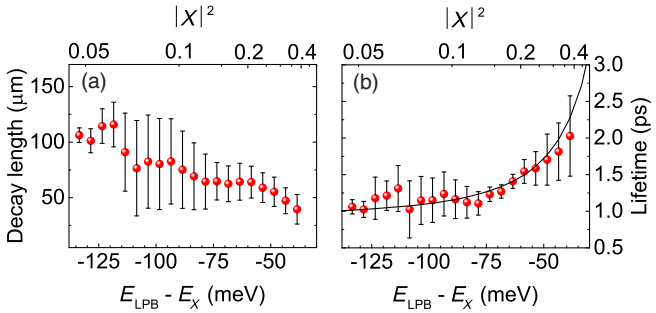

FIG. 5. Low-temperature decay of waveguided polaritons. (a) Polariton decay length as a function of the polariton energy. The mean value and error bars are deduced from a set of several measurements taken between 4 and 30 K. No substantial difference in the lifetime and the decay length is observed within this temperature range. (b) Lifetime of the guided polaritons. Measured data (the red dots) and fit to Eq. (4) (the black line). The top axis in both graphs represents the excitonic fraction of polaritons at the corresponding LPB energy.

the excitation spot is reduced by a factor of e—and hence their lifetime, the measured integrated PL intensity is multiplied by the propagation distance, which is fitted to an exponential decay. The obtained decay length as a function of the polariton energy is shown in Fig. 5(a). Polaritons with a large photonic fraction in excess of 0.94 are characterized by a decay length larger than 100 μm, which decreases as the excitonic fraction becomes larger. To further support this analysis, the absorption coefficient in the waveguide is determined by the variable-stripe-length method to be 60 cm^{-1} at around 200 meV below the free X_A energy [11], which corresponds to a decay length of 167 μm. This decay length puts an upper limit to the propagation length of the photons and highly photonic polaritons in the present sample and is mainly limited by residual absorption in the waveguide. We can expect the absorption to be higher—and the corresponding decay length lower—for higher energies. Since the value of 167 μm only slightly exceeds the measured polariton decay lengths at energies between 120 and 140 meV below X_A, absorption is most likely the limiting factor of polariton propagation. The absorption losses could be reduced by increasing the Al content in the QW barriers, thus shifting the band edge up.

Another essential figure of merit to qualify the present structure is the polariton lifetime $\tau_{\mathrm{pol}}(\beta)$. The latter is given by

$$\frac{1}{\tau_{\mathrm{pol}}(\beta)} = \frac{|P(\beta)|^2}{\tau_p} + \frac{|X(\beta)|^2}{\tau_X}, \tag{4}$$

where τ_p and τ_X are the photon and exciton lifetimes, respectively, P and X are the usual Hopfield coefficients, and $|P(\beta)|^2$ and $|X(\beta)|^2$ give the photon and exciton fraction of the polaritons, respectively [48]. The polariton lifetime $\tau_{\mathrm{pol}}(\beta)$ is determined by dividing the measured polariton decay length by the group velocity of the LPB, defined as $\partial\omega/\partial\beta$ [Fig. 5(b)]. Values ranging between 1 and 2 ps are derived for polaritons with an exciton fraction between 0.05 and 0.4. The free-X_A lifetime is determined by time-resolved PL to be 325 ps at $T = 10$ K. A fit from Eq. (4) to the data leads to a value of 0.9 ps for τ_p, which corresponds to a photonic linewidth of $\gamma_P = 0.73$ meV and an optical quality factor of 4.9×10^3. This photonic lifetime is about a factor of 5 larger than that reported for comparable III-nitride planar MCs [49], essentially due to the improved confinement provided by TIR. Note that we do not directly observe the photonic and excitonic linewidths stated above in the measured-dispersion signal for highly photonic and excitonic polaritons, respectively. In addition to this broadening along the energy axis, there is indeed an extra source of broadening in the emission angle due to fabrication inhomogeneities in the grating coupler. For highly photonic polaritons, the energy linewidth becomes relatively small and the observed signal broadening is of purely angular origin. In this limit, we observe an angular full width at half maximum (FWHM) linewidth $\Delta\alpha$ of 1.2°, which corresponds to a FWHM wave-vector linewidth Δk_z of 0.34 $\mu\mathrm{m}^{-1}$ and a FWHM error on the grating period $\Delta\Lambda = 0.8$ nm through Eq. (2). The normal-mode splitting of 60 meV corresponds to a Rabi period, i.e., the period of the coherent oscillations between the photon and exciton fractions of the polariton, as short as 69 fs. In this respect, we point out that the present sample is characterized by a large polariton-lifetime-to-Rabi-period ratio. When comparing the present values to those obtained in GaAs-based waveguides [14], the shorter decay lengths and lifetimes in III-nitride structures are likely due to the combination of an enhanced sensitivity to photonic disorder of short wavelength systems together with the increased residual absorption in the waveguide. If we compare the obtained values for the decay length to the ballistic condensate propagation on the order of 10 μm reported by Hahe *et al.* in a ZnO planar MC [50], the much larger decay length in the present case can be well accounted for by TIR confinement and the larger polariton propagation velocity.

Additional information on the temperature dependence of the SCR can be obtained by considering the relation

$$\Omega_{\mathrm{Rabi}}(T) = \sqrt{4g_0^2 - [\gamma_{\mathrm{hom}}^{X_A}(T) - \gamma_P]^2}, \tag{5}$$

which is derived from the COM [11]. We assume the photonic linewidth γ_P to be temperature independent. The homogeneous excitonic linewidth of the X_A exciton, $\gamma_{\mathrm{hom}}^{X_A}(T)$, is extracted by fitting a Voigt peak profile to the temperature-dependent PL data shown in Fig. 3(a). Note that we take only the homogeneous broadening into account since the normal-mode splitting does not depend on the inhomogeneous broadening when the normal-mode

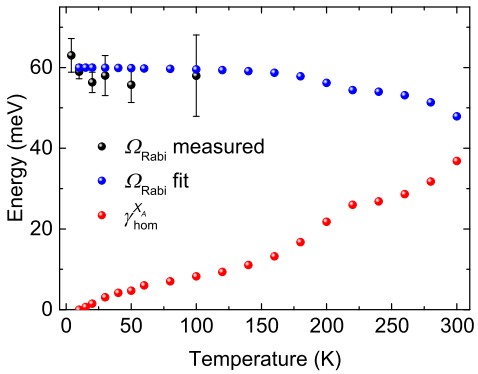

FIG. 6. Temperature dependence of Ω_{Rabi}. Measured values (the black dots) and extrapolation up to room temperature (the blue dots) from Eq. (5), calculated using the homogeneous X_A-exciton linewidth obtained from the measurements shown in Fig. 3(a) (the red dots).

splitting to MQW inhomogeneous broadening ratio is large [51,52]. The calculated values of $\Omega_{\mathrm{Rabi}}(T)$ are shown in Fig. 6, together with $\gamma_{\mathrm{hom}}^{X_A}(T)$. Based on these calculations, we can predict a slight decrease in the normal-mode splitting down to 48 meV at 300 K. This finding again confirms the strong potential of the present platform to investigate the SCR up to room temperature.

V. CONCLUSION AND OUTLOOK

In this paper, we demonstrate propagating polaritons in III-nitride slab waveguides, where c-plane GaN/(Al, Ga)N MQW excitons hybridize with the propagating TE_0 optical mode. The fully lattice-matched growth leads to a very low disorder and high in-plane homogeneity. The SCR is observed up to 100 K with an average normal-mode splitting as high as 60 meV due to the large overlap between the QWs and the waveguide mode. The guided polaritons feature a decay length of 50 to 100 μm and a lifetime of 1 to 2 ps, which are well accounted for by residual absorption in the waveguide. Absorption losses could be reduced by increasing the Al content in the barriers.

Such a structure shows great potential for photonic and polaritonic integrated circuits up to room temperature. In this perspective, ridge waveguides with lateral confinement would prove a more practical geometry for devices, as it would prevent the isotropic propagation of the polaritons. Consequently, the signature of waveguided polaritons should be measurable over longer distances and up to higher temperatures. It would also open the possibility of exploring polariton nonlinearities, e.g., polariton-soliton wave packets up to room temperature.

ACKNOWLEDGMENTS

We would like to thank the Swiss National Science Foundation for its financial support through Grant No. 200020_162657.

[1] D. A. B. Miller, Device requirements for optical interconnects to silicon chips, Proc. IEEE **97**, 1166 (2009).
[2] S. I. Pekar, Theory of electromagnetic waves in a crystal with excitons, J. Phys. Chem. Solids **5**, 11 (1958).
[3] T. C. H. Liew, A. V. Kavokin, and I. A. Shelykh, Optical Circuits Based on Polariton Neurons in Semiconductor Microcavities, Phys. Rev. Lett. **101**, 016402 (2008).
[4] A. Amo, T. C. H. Liew, C. Adrados, R. Houdré, E. Giacobino, A. V. Kavokin, and A. Bramati, Exciton-polariton spin switches, Nat. Photonics **4**, 361 (2010).
[5] R. W. Boyd, *Nonlinear Optics*, Nonlinear Optics Series (Academic Press, Cambridge, MA, 2008).
[6] G. A. Wurtz and A. V. Zayats, Nonlinear surface plasmon polaritonic crystals, Laser Photonics Rev. **2**, 125 (2008).
[7] P. M. Walker, L. Tinkler, D. V. Skryabin, A. Yulin, B. Royall, I. Farrer, D. A. Ritchie, M. S. Skolnick, and D. N. Krizhanovskii, Ultra-low-power hybrid light-matter solitons, Nat. Commun. **6**, 8317 (2015).
[8] C. Weisbuch, M. Nishioka, A. Ishikawa, and Y. Arakawa, Observation of the Coupled Exciton-Photon Mode Splitting in a Semiconductor Quantum Microcavity, Phys. Rev. Lett. **69**, 3314 (1992).
[9] V. Savona, L. C. Andreani, P. Schwendimann, and A. Quattropani, Quantum well excitons in semiconductor microcavities: Unified treatment of weak and strong coupling regimes, Solid State Commun. **93**, 733 (1995).
[10] M. Fox, *Quantum Optics: An Introduction*, *Oxford Master Series in Atomic, Optical, and Laser Physics Vol. 15* (Oxford University Press, New York, 2006).
[11] See Supplemental Material at http://link.aps.org/supplemental/10.1103/PhysRevApplied.7.034019 for relevant details on (i) the definition of L_{eff}, (ii) XRD measurements, (iii) parameters used for the $k \cdot p$ calculations, (iv) experimental details of the optical measurements, (v) time-resolved-photoluminescence data, (vi) a sketch of the radial outspread of the polaritons, (vii) raw dispersion data at 4 and 100 K, (viii) the employed coupled-oscillator model and details about the FDTD calculations, and (ix) the variable-stripe-length method and corresponding results.
[12] T. Ellenbogen and K. B. Crozier, Exciton-polariton emission from organic semiconductor optical waveguides, Phys. Rev. B **84**, 161304(R) (2011).
[13] H. Takeda and K. Sakoda, Exciton-polariton mediated light propagation in anisotropic waveguides, Phys. Rev. B **86**, 205319 (2012).
[14] P. M. Walker, L. Tinkler, M. Durska, D. M. Whittaker, I. J. Luxmoore, B. Royall, D. N. Krizhanovskii, M. S. Skolnick, I. Farrer, and D. A. Ritchie, Exciton polaritons in semiconductor waveguides, Appl. Phys. Lett. **102**, 012109 (2013).
[15] S. Pirotta, M. Patrini, M. Liscidini, M. Galli, G. Dacarro, G. Canazza, G. Guizzetti, D. Comoretto, and D. Bajoni, Strong coupling between excitons in organic semiconductors and Bloch surface waves, Appl. Phys. Lett. **104**, 051111 (2014).
[16] D. D. Solnyshkov, H. Terças, and G. Malpuech, Optical amplifier based on guided polaritons in GaN and ZnO, Appl. Phys. Lett. **105**, 231102 (2014).
[17] I. Rosenberg, Y. Mazuz-Harpaz, R. Rapaport, K. West, and L. Pfeiffer, Electrically controlled mutual interactions of flying waveguide dipolaritons, Phys. Rev. B **93**, 195151 (2016).

[18] C. Antón, T. C. H. Liew, G. Tosi, M. D. Martín, T. Gao, Z. Hatzopoulos, P. S. Eldridge, P. G. Savvidis, and L. Viña, Dynamics of a polariton condensate transistor switch, Appl. Phys. Lett. **101**, 261116 (2012).
[19] C. Antón, T. C. H. Liew, G. Tosi, M. D. Martín, T. Gao, Z. Hatzopoulos, P. S. Eldridge, P. G. Savvidis, and L. Viña, Energy relaxation of exciton-polariton condensates in quasi-one-dimensional microcavities, Phys. Rev. B **88**, 035313 (2013).
[20] G. Christmann, R. Butté, E. Feltin, A. Mouti, P. A. Stadelmann, A. Castiglia, J.-F. Carlin, and N. Grandjean, Large vacuum Rabi splitting in a multiple quantum well GaN-based microcavity in the strong-coupling regime, Phys. Rev. B **77**, 085310 (2008).
[21] Lumerical Solutions, Inc., FDTD Solutions v. 8.11.422.
[22] D. Brunner, H. Angerer, E. Bustarret, F. Freudenberg, R. Höpler, R. Dimitrov, O. Ambacher, and M. Stutzmann, Optical constants of epitaxial AlGaN films and their temperature dependence, J. Appl. Phys. **82**, 5090 (1997).
[23] R. Butté, E. Feltin, J. Dorsaz, G. Christmann, J.-F. Carlin, N. Grandjean, and M. Ilegems, Recent progress in the growth of highly reflective nitride-based distributed Bragg reflectors and their use in microcavities, Jpn. J. Appl. Phys. **44**, 7207 (2005).
[24] G. Cosendey, J.-F. Carlin, N. A. K. Kaufmann, R. Butté, and N. Grandjean, Strain compensation in AlInN/GaN multilayers on GaN substrates: Application to the realization of defect-free Bragg reflectors, Appl. Phys. Lett. **98**, 181111 (2011).
[25] G. Perillat-Merceroz, G. Cosendey, J.-F. Carlin, R. Butté, and N. Grandjean, Intrinsic degradation mechanism of nearly lattice-matched InAlN layers grown on GaN substrates, J. Appl. Phys. **113**, 063506 (2013).
[26] A. Castiglia, J.-F. Carlin, E. Feltin, G. Cosendey, J. Dorsaz, and N. Grandjean, Emission characteristics of GaN-based blue lasers including a lattice matched $Al_{0.83}In_{0.17}N$ optical blocking layer for improved optical beam quality, Appl. Phys. Lett. **97**, 111104 (2010).
[27] N. Grandjean, B. Damilano, S. Dalmasso, M. Leroux, M. Laügt, and J. Massies, Built-in electric-field effects in wurtzite AlGaN/GaN quantum wells, J. Appl. Phys. **86**, 3714 (1999).
[28] E. Feltin, J.-F. Carlin, J. Dorsaz, G. Christmann, R. Butté, M. Laügt, M. Ilegems, and N. Grandjean, Crack-free highly reflective AlInN-AlGaN Bragg mirrors for UV applications, Appl. Phys. Lett. **88**, 051108 (2006).
[29] D. Taillaert, F. Van Laere, M. Ayre, W. Bogaerts, D. Van Thourhout, P. Bienstman, and R. Baets, Grating couplers for coupling between optical fibers and nanophotonic waveguides, Jpn. J. Appl. Phys. **45**, 6071 (2006).
[30] S. L. Chuang and C. S. Chang, $k \cdot p$ method for strained wurtzite semiconductors, Phys. Rev. B **54**, 2491 (1996).
[31] F. Bernardini and V. Fiorentini, Spontaneous versus piezoelectric polarization in III-V nitrides: Conceptual aspects and practical consequences, Phys. Status Solidi (b) **216**, 391 (1999).
[32] R. P. Leavitt and J. W. Little, Simple method for calculating exciton binding energies in quantum-confined semiconductor structures, Phys. Rev. B **42**, 11774 (1990).
[33] D. E. Aspnes, Third-derivative modulation spectroscopy with low-field electroreflectance, Surf. Sci. **37**, 418 (1973).
[34] M. Glauser, C. Mounir, G. Rossbach, E. Feltin, J.-F. Carlin, R. Butté, and N. Grandjean, InGaN/GaN quantum wells for polariton laser diodes: Role of inhomogeneous broadening, J. Appl. Phys. **115**, 233511 (2014).
[35] E. Feltin, D. Simeonov, J.-F. Carlin, R. Butté, and N. Grandjean, Narrow UV emission from homogeneous GaN/AlGaN quantum wells, Appl. Phys. Lett. **90**, 021905 (2007).
[36] F. Stokker-Cheregi, A. Vinattieri, E. Feltin, D. Simeonov, J. Levrat, J.-F. Carlin, R. Butté, N. Grandjean, and M. Gurioli, Impact of quantum confinement and quantum confined Stark effect on biexciton binding energy in GaN/AlGaN quantum wells, Appl. Phys. Lett. **93**, 152105 (2008).
[37] R. Cingolani, G. Coli', R. Rinaldi, L. Calcagnile, H. Tang, A. Botchkarev, W. Kim, A. Salvador, and H. Morkoç, Optical properties of $GaN/Al_xGa_{1-x}N$ quantum wells, Phys. Rev. B **56**, 1491 (1997).
[38] C. Weisbuch (private communication).
[39] L. Viña, S. Logothetidis, and M. Cardona, Temperature dependence of the dielectric function of germanium, Phys. Rev. B **30**, 1979 (1984).
[40] G. Rossbach, J. Levrat, E. Feltin, J.-F. Carlin, R. Butté, and N. Grandjean, Impact of saturation on the polariton renormalization in III-nitride based planar microcavities, Phys. Rev. B **88**, 165312 (2013).
[41] Since we do not observe any spectral signature in the polariton-dispersion data that could be related to the X_B exciton, such as the presence of a middle polariton branch, we fully neglect X_B in the analysis and the modeling of the dispersion curves.
[42] F. Tassone, C. Piermarocchi, V. Savona, A. Quattropani, and P. Schwendimann, Bottleneck effects in the relaxation and photoluminescence of microcavity polaritons, Phys. Rev. B **56**, 7554 (1997).
[43] P. Corfdir, J. Levrat, G. Rossbach, R. Butté, E. Feltin, J.-F. Carlin, G. Christmann, P. Lefebvre, J.-D. Ganière, N. Grandjean, and B. Deveaud-Plédran, Impact of biexcitons on the relaxation mechanisms of polaritons in III-nitride based multiple quantum well microcavities, Phys. Rev. B **85**, 245308 (2012).
[44] G. Christmann, R. Butté, E. Feltin, J.-F. Carlin, and N. Grandjean, Room temperature polariton lasing in a GaN/AlGaN multiple quantum well microcavity, Appl. Phys. Lett. **93**, 051102 (2008).
[45] T. Guillet, M. Mexis, J. Levrat, G. Rossbach, C. Brimont, T. Bretagnon, B. Gil, R. Butté, N. Grandjean, and L. Orosz, Polariton lasing in a hybrid bulk ZnO microcavity, Appl. Phys. Lett. **99**, 161104 (2011).
[46] L. Tinkler, Ph.D. thesis, University of Sheffield, 2015.
[47] C. Sturm, D. Tanese, H. S. Nguyen, H. Flayac, E. Galopin, A. Lemaître, I. Sagnes, D. Solnyshkov, A. Amo, G. Malpuech, and J. Bloch, All-optical phase modulation in a cavity-polariton Mach-Zehnder interferometer, Nat. Commun. **5**, 3278 (2014).
[48] J. J. Hopfield, Theory of the contribution of excitons to the complex dielectric constant of crystals, Phys. Rev. **112**, 1555 (1958).

[49] J. Levrat, R. Butté, E. Feltin, J.-F. Carlin, N. Grandjean, D. Solnyshkov, and G. Malpuech, Condensation phase diagram of cavity polaritons in GaN-based microcavities: Experiment and theory, Phys. Rev. B **81**, 125305 (2010).

[50] R. Hahe, C. Brimont, P. Valvin, T. Guillet, F. Li, M. Leroux, J. Zuniga-Perez, X. Lafosse, G. Patriarche, and S. Bouchoule, Interplay between tightly focused excitation and ballistic propagation of polariton condensates in a ZnO microcavity, Phys. Rev. B **92**, 235308 (2015).

[51] R. Houdré, R. P. Stanley, and M. Ilegems, Vacuum-field Rabi splitting in the presence of inhomogeneous broadening: Resolution of a homogeneous linewidth in an inhomogeneously broadened system, Phys. Rev. A **53**, 2711 (1996).

[52] G. Christmann, R. Butté, E. Feltin, J.-F. Carlin, and N. Grandjean, Impact of inhomogeneous excitonic broadening on the strong exciton-photon coupling in quantum well nitride microcavities, Phys. Rev. B **73**, 153305 (2006).